Supporting Information

Coherent Nanotwins and Dynamic Disorder in Cesium Lead Halide Perovskite Nanocrystals

Federica Bertolotti, Loredana Protesescu, Maksym V. Kovalenko, Sergii Yakunin, Antonio Cervellino, Simon J. L. Billinge, Maxwell W. Terban, Jan Skov Pedersen, Norberto Masciocchi* and Antonietta Guagliardi*

*To whom correspondence should be addressed: antonella.guagliardi@ic.cnr.it

Supplementary Methods

1. Synchrotron X-ray Total Scattering data collection and reduction.
2. Crystal structure refinement by the Rietveld method.
3. The Debye Scattering Equation method.
4. Modelling twin boundaries in $CsPbX_3$ NCs by the DSE method.
5. High-energy X-ray scattering data collection and Pair Distribution Function modelling.
6. Energetic considerations on the formation of twin boundaries.
7. Small Angle X-Ray Scattering.

Supplementary Figures

Figures S1-S8

Supplementary Tables

Tables S1-S5

Supplementary Methods

1. Synchrotron X-ray Total Scattering data collection and reduction.

$CsPbX_3$ samples, both as colloidal suspensions (in toluene or hexane) and dry powders, synthesized according to Protesescu et al.,[1] were loaded into borosilicate glass capillaries with certified composition (Hilgenberg GmbH 0500), 0.8 mm in diameter.

High-resolution Wide Angle X-ray Total Scattering (WAXTS) measurements have been performed at the X04SA-MS4 Powder Diffraction Beamline of the Swiss Light Source (Paul Scherrer Institute, Villigen, CH).[2]

Two different beam energies of 25 KeV and 22 KeV were set and the operational wavelengths (λ_{25KeV} = 0.495476 Å, λ_{22KeV} = 0.565483 Å) accurately determined using a silicon powder standard (NIST 640d, a_0 = 0.543123(8) nm at 22.5°C). Data were collected in the 0.5°-130° 2θ range using a single-photon counting silicon microstrip detector (MYTHEN II).[3] A temperature-controlled N_2 stream fluxing on the capillaries was used for low- and high-temperature data collection. He/air background, empty glass capillary and pure solvent WAXTS patterns were independently collected under the same experimental conditions.

Angle-dependent intensity corrections were applied to the raw data to account for sample attenuation due to absorption effects;[4] sample absorption curves were determined by measuring the transmitted beam from the filled capillaries, while for the empty capillaries the X-ray attenuation coefficient was computed using their nominal composition. Angular calibrations were applied to the zero angle and to x, y capillary offsets, derived from the certified silicon powder standard (NIST 640d) using locally developed procedures. Air and (absorption-corrected) capillary scattering contributions were subtracted from the sample signals; absorption corrected solvent patterns (hexane and toluene) were subtracted for Rietveld analysis, whereas they were used as additional components to the DSE models, as well as the inelastic Compton scattering contribution.

2. Crystal structure refinement by the Rietveld method.

For $CsPbCl_3$ colloidal nanocrystals (NCs) and dry powders, several structural models have been tested (details are given in Supplementary Table S1) on synchrotron data collected at RT:

i) The cubic archetypal perovskite structure (S.G. *Pm-3m*), as reported in ref. 5, giving unphysical Atomic Displacement Parameters (ADPs) for the Cl atoms (as detailed in the main text).

ii) A cubic model (S.G. *Pm-3m*) with Cl atoms displaced from the ½,0,0 crystallographic site of *4/mm.m* symmetry (Wyckoff *d* site) by *ca.* 0.51 Å (½ , 0.0903(4), 0, Wyckoff *h* site of *mm2..* symmetry), and with a fractional s.o.f. of 1/4, being split into four equivalent crystallographic positions. This model supplied reasonable ADPs, but unphysical bond angles within the $PbCl_6$ octahedra.

iii) An orthorhombic model (S.G. *Pbnm*), with axial lengths of √2:√2:2 times that of the cubic lattice, providing both reasonable ADPs and molecular geometry, but manifesting the presence of weak, but clearly visible, superstructure peaks in the 1.5-2 Q $Å^{-1}$ range, not observed in the experimental data.

For data collected below RT, from 223 K down to 133 K, results from the cubic archetypal perovskite structure (S.G. *Pm-3m*) providing the ADPs parameters reported in Figure 3 of the main text are given in Supplementary Table S2. Best fits from Rietveld analysis are shown in Supplementary Figure S1 for some data.

Rietveld refinement has been performed on RT WAXTS data collected on $CsPbBr_3$ colloidal and dry samples, testing the deposited orthorhombic *Pbnm* γ-phase bulk structure[6] and a tetragonal *P4/mbm* β-phase (motivated by the apparent pseudo-tetragonal features in the 1.5-2 Q $Å^{-1}$ range, observed in many batches). Depending on the sample, the orthorhombic structure provided better or competitive agreement indexes, compared to the tetragonal one. Worth noting, the extent of the orthorhombic distortion derived here for $CsPbBr_3$ NCs is very similar to that reported for the bulk by Rodova et al.[6] The smallest samples (such as the colloidal NCs shown in Figure 2 in the main text and in Table S3), exhibited a refined cell volume slightly larger than in the bulk (802.7 $Å^3$ *vs.* 796.7 $Å^3$, respectively), likely a consequence of the well-known size-dependent volume expansion occurring at the nanoscale for non-metallic species.[7]

Rietveld refinement has also been performed on data collected on a powder sample above and below RT, at different T values. We show here some of the best fits (Figure S1) at LT and RT, with the orthorhombic *Pbnm* γ-phase, and on data at 410 K, with the cubic model.

Figure S2 shows the analysis on the peak positions of HT $CsPBBr_3$, indicating the deviations from the cubic symmetry.

Starting from the refined structural model of $CsPbBr_3$, the final coordinates for the isostructural orthorhombic $CsPbI_3$ γ-phase have been derived within the *Pbnm* symmetry constraints against the experimental synchrotron data (best fit shown in Figure 5 of the main text). Cell parameters and coordinates of colloidal $CsPbBr_3$ and $CsPbI_3$ are reported in Supplementary Table S3. The orthorhombic *Pbnm* γ-phase used for the DSE twin model of the HT (pseudo-cubic) data of $CsPbBr_3$ is isostructural with the RT phase.

All computations have been performed by TOPAS-R (v3.0, 2005, Bruker AXS, Karlsruhe, Germany).

3. The Debye Scattering Equation method.

The DSE provides the average differential cross section (or the powder diffraction pattern) of a randomly oriented powder from the distribution of interatomic distances between atomic pairs, without any assumption of periodicity and order:

$$I(Q) = \sum_{j=1}^{N} f_j(Q)^2 o_j^2 + 2\sum_{j>i}^{N} f_j(Q) f_i(Q) T_j(Q) T_i(Q) o_j o_i \frac{\sin{(Qd_{ij})}}{(Qd_{ij})}$$

where $Q = \frac{4\pi sin\theta}{\lambda}$ is the magnitude of the scattering vector, λ is the radiation wavelength, f_i is the X-ray atomic form factor of element i, d_{ij} is the interatomic distance between atoms i and j, N is the total number of atoms and T and o are the thermal atomic displacement parameter and the site occupancy factor associated to each atomic species, respectively. The first summation in the above equation includes the contributions of the zero distance between one atom and itself and the second term (the interference term) the non-zero interatomic distances $d_{ij} = | r_i - r_j |$.

This approach, compared to the conventional Rietveld method, takes advantage of the simultaneous modelling of Bragg and diffuse scattering and thus enables an appropriate description of the Total Scattering of samples when: *i)* a limited extension of the coherent domains, *ii)* the occurrence of local structural defects and *iii)* various kinds of compositional disorders are present, within an approach nearly free of phenomenological components. In addition, unlike the Pair Distribution Function (PDF) method, the DSE does not require the *sine*-Fourier Transform of the experimental data, thus resorting to high-energy X-rays (> 30 keV) is not mandatory.

A complete DSE analysis protocol has been recently implemented in an open source program package (the *DebUsSy* program Suite).[8] Thanks to some smart computational tricks, such as reducing the number of interatomic distances by fully exploiting the crystal symmetry, and using sampled interatomic distances instead of the original ones,[9] this computationally heavy approach becomes feasible.

The Suite relies on a bottom-up approach that consists of two main steps. In the first one, a mono- or bivariate population of atomistic models of nanocrystals (NCs) with increasing size and desired shape are generated, with the set of multiplicities of sampled interatomic distances stored in suitable databases. In the second step, this stored information is used to compute the DSE and a number of model parameters are refined against the experimental data. Mono- or bivariate lognormal NCs size distributions are used,[10] characterized by average values and widths (or standard deviations).

The DSE modelling strategy was here firstly applied to deal with the average (untwinned) crystal structure of $CsPbX_3$ NC. This strategy is summarized below:

i) A bivariate population of NCs has been generated for each structural model (cubic tetragonal and orthorhombic – as provided by the Rietveld analysis described in section 2), according to two independent growth directions, one parallel to the ab-plane and the other along c-axis, to deal with NCs of anisotropic shapes. The unit cell setting was properly transformed to account for the observed NCs morphology. Each NC was built by generating a framework of lattice nodes enclosed within a geometrical (prismatic) surface and by convoluting each node with the Patterson vectors within the unit cell. Each population built in this way includes all possible combinations of bases (or their equivalent diameters) and heights, the size steps between two consecutive NCs being the diameter of the circle of equivalent area to the unit cell-base $[ab]$ and the c lattice parameter, respectively. For $CsPbI_3$ NCs, the b-lattice parameter was doubled in order to account for an aspect ratio of 1:2 in the ab-plane, which resulted in a better fit of the experimental data.

ii) The Simplex algorithm was used to optimize the initial model parameters against the experimental data.[11] Information from TEM and Small Angle X-ray Scattering were used to constrain the average size and the standard deviation of the log-normal distribution. Isotropic Debye Waller factors were refined for each crystallographically independent atom. ADPs resulted in very good agreement with those provided by the Rietveld analysis. Some graphical output of this DSE-based analysis is shown in Figure S3.

For colloidal samples the solvent scattering contribution (toluene or hexane) was taken into account by using the experimental trace (independently collected for pure solvent) as a blank curve, scaled by linear least squares as an additional component of the pattern model.

4. Modelling twin boundaries in $CsPbX_3$ NCs by the DSE method.

The vanishing of superstructure peaks in the powder diffraction pattern of cubic lead halide perovskites at room- ($CsPbCl_3$) and high-temperatures ($CsPbBr_3$ and $CsPbI_3$) is here interpreted as the occurrence of planar structural defects along the crystallographic directions corresponding to the missing reflections in reciprocal space. The coherence of the lattice throughout the NCs is, however, maintained over the boundaries between different domains, as witnessed by the agreement between the nanoparticle sizes observed by HRTEM, SAXS and those derived through the Debye Function Analysis, as reported in Table 2 of the main text.

In order to test the effects of different twin boundaries on the $CsPbX_3$ diffraction patterns, we considered planar defects joining together nanocrystalline domains related by crystallographic mirror planes. As these defects break the long-range periodicity of the NCs, the DSE method was used, enabling the computation of the X-ray powder diffraction pattern without any assumption of periodicity and order.[8,12]

In order to generate the twin boundaries in the orthorhombic phase of $CsPbX_3$ NCs, a proper slip system was added to the atomistic models by shifting the atoms according to the required twin law: $k < hkl > \{hkl\}$, being k the magnitude of the shift, $< hkl >$ the direction (including all the symmetry equivalent ones) and $\{hkl\}$ all the equivalent families of the planes of the twin boundary. Different simulations were performed aiming at selecting the appropriate magnitude, direction and plane of the dislocation slips, resulting into the precise disappearance of the superstructure peaks along the crystallographic direction of the related planar defect (see Figure S4). This brings to the fundamental consideration that, by simply analysing the experimental WAXTS data of $CsPbX_3$, it is possible to infer the precise direction of the twin boundary that breaks the crystal periodicity and generates the multi-domains structures extensively described in the main text.

- The twin boundaries model of pseudo-cubic $CsPbCl_3$ NCs

The absence of superstructure peaks in the RT pseudo-cubic X-ray powder diffraction patterns of $CsPbCl_3$ (colloidal and gel samples) makes the identification of an univocal defective atomistic model not an easy task. In this case, we assumed that twin boundaries, for $\frac{1}{2} < 110 > \{110\}$ slip system, occur along all the allowed crystallographic directions within the orthorhombic reference frame. Therefore, it is intended that, taking the $\frac{1}{2} < 110 > \{110\}$ labeling, for a single (110) slip plane, the directions of the shift can be [-110] (and [1-10]), but not [110] nor [-1-10] or, in other words, shifts must be within the slip plane. A 100% percentage of defective clusters resulted in the best fit shown in Figure 3 of the main text. The adopted slip system has been observed in many perovskite-type structures, as reported in ref. 13.

- The twin boundaries model of RT and HT $CsPbBr_3$ NCs

In the $CsPbBr_3$ data collected at RT (Figure S4a) the superstructure peak at ~ 1.8 Å^{-1} is missing, resulting in a pseudo-tetragonal average symmetry. A single twin boundary suitably located in the orthorhombic structure is the minimal number of slips for generating such effect on the diffraction pattern, as demonstrated in the following. Since only coherent twin boundaries are considered, the possible combinations of slip geometries are:

a) ½ $< 110 > \{110\}$: slip planes $\{110\}$, along the $< 110 >$ directions with a shift of $\frac{1}{2}\sqrt{a^2 + b^2}$ (half of the diagonal of the *Pbnm* unit cell). Figure S4b shows the effect of this defect, demonstrating that the superstructure peaks with larger hk components are mainly affected, resulting in a misfit of the experimental trace (particularly at 1.7 and 2.0 Å^{-1}).

b) ½ $< 100 > \{001\}$: slip planes $\{001\}$, along the $< 100 >$ directions with a shift of $\frac{1}{2}a$ (half of the a lattice parameter). As illustrated in Figure S4c, peaks out of the superstructure peak region are heavely distorted by this type of twin boundary, resulting into a worst match than that of the orthorhombic periodic structure. The same effect is observed for a ½ $< 010 > \{001\}$ slip geometry.

c) ½ $< 110 > \{001\}$: slip planes $\{001\}$, along the $< 110 >$ directions with a shift as in the case a). As shown in Figure S4d, this slip geometry results in a misfit of the experimental trace (particularly at 2.0 Å^{-1}).

d) ½ $< 001 > \{110\}$: slip planes $\{110\}$ along the $< 001 >$ directions with a shift of $\frac{1}{2}c$ (half of the c lattice parameter). Figure 4 of the main text shows that this slip system, breaking the periodicity along <001>, causes the vanishing of the superstructure peak at ~ 1.8 Å^{-1}, reproduces the observed pseudo-tetragonal crystal symmetry in $CsPbBr_3$.

In order to improve the match with the experimental data, the final model was built by suitably weighting twinned (70%) and untwinned NCs. The final model highlights the dynamic nature of the perovskite crystal structure, not fully tetragonal neither orthorhombic in RT $CsPbBr_3$ NCs.

Owing to the pseudo-cubic symmetry of the HT diffraction pattern of $CsPbBr_3$, the same considerations made for $CsPbCl_3$ are still valid; furthermore, the $\frac{1}{2} < 110 > \{110\}$ slip system in this case was not enough to explain the intensity ratio of the 121 (Q = 1.5 Å^{-1}) and 202 (Q = 2.2 Å^{-1}) reflections. Such intensity modulation is obtained by further adding the ½ $< 100 > \{001\}$ slip system. The best fit of the HT experimental data of $CsPbBr_3$ (shown in Figure 4 of the main text) was obtained by weighting $\frac{1}{2} < 110 > \{110\}$ (80%) and $\frac{1}{2} < 100 > \{001\}$ (20%) slip systems.

5. High-energy X-ray scattering data collection and Pair Distribution Function modelling.

High-energy X-ray WAXTS data of $CsPbBr_3$ (as dry powder) were collected at the 28-ID-1 XPD beamline at National Synchrotron Light Source II (NSLS-II) at Brookhaven National Laboratory (Upton, NY, US). The measurements were performed at room temperature using an X-ray energy of 67 keV ($\lambda = 0.1827$ Å), as required to reduce the truncation errors associated to the *sine*-Fourier Transform of the experimental data into real space. The powder was loaded into a kapton capillary (1.0 mm in diameter) and sealed with clay and epoxy. The experimental data were measured using the Rapid Acquisition PDF mode on a silicon-based 2D detector,[14] collecting scattering data up to a momentum transfer $Q_{max} = 23$ Å^{-1}. A microcrystalline nickel sample was used to calibrate the experimental setup (operational wavelength, sample-to-detector distance, detector tilting) using Fit2D[14], by which all the 2D diffraction images were integrated to 1D intensities *vs.* Q. The Total Scattering Function *S(Q)* was obtained from the 1D X-ray pattern, using the PDFgetX3 program.[15] The *sine*-Fourier transform is then applied on the reduced Total Scattering Structure Function, $F(Q) = Q[S(Q) - 1]$, obtaining the **experimental** *G(r)*, which gives the probability of finding an atom at a distance *r* away from another:

$$G(r) = \frac{2}{\pi}\int_{Q_{min}}^{Q_{max}} Q[S(Q) - 1]\sin Qr \ \mathrm{d}Q$$

where $Q = \frac{4\pi sin\theta}{\lambda}$ is the magnitude of the scattering vector, $Q_{min} = 0.1$ Å^{-1} is the lowest accessible Q value (limited by the presence of the beamstop) and $Q_{max} = 23.0$ Å^{-1}.

Using the PDFGUI approach,[16] the **model** *G(r)* is computed starting from the unit cell of the structure and refined against the experimental one, by adjusting a certain number of parameters (see below) and with the spherical envelope approximation,[17] describing a faster decay of the PDF with *r*, with respect to the corresponding microcrystalline material.

In order to explore the presence of smaller coherent orthorhombic domains resulting into a medium-order range tetragonal structure in our dry $CsPbBr_3$ NCs, we divided the whole accessible *r*- range (2-70Å) in two separated intervals (2-26 Å and 26-70 Å); after refining, over the whole *r* range, the unit cell parameters, atomic coordinates and Debye-Waller factors (considering the axial Br_1 and equatorial Br_2 atoms as independent atomic species) for both structural models, we calculated the agreement index for each structure for each section. As detailed in the main text, we found that the orthorhombic structure fits well the low *r* section ($R_{w,\text{ orthorhombic}} = 12.9\%$ *vs.* $R_{w,\text{ tetragonal}} = 18.5\%$), whereas a tetragonal description has to be preferred in the 26–70 Å range ($R_{w,\text{ orthorhombic}} = 12.4\%$ *vs.* $R_{w,\text{ tetragonal}} = 10.9\%$).

6. Energetic considerations on the formation of twin boundaries

The Gibbs free energy G = H – TS, where the enthalpy H and the entropy S both contribute, determines the thermodynamic equilibrium state at any given T. The configurational entropy term (per unit volume), after appearance of a network of twin boundaries (separating N small ordered nanodomains of volume $v = N^{-1}$), can be shown to be $S = N\,k_B \ln m$, where m is the number of different possible twin individual orientations ($m > 1$), and k_B is the Boltzmann's constant (R. Kubo, *Statistical Mechanics*, 2nd ed., Chap. 5, North Holland, New York, 1993). Therefore, a progressive subdivision in ordered subdomains is entropically favored at high T by the higher S, even if the (unknown) energetic cost of creating the necessary boundary network would be high. As these boundaries, through surface tension, contribute to increase the overall G by a *positive* term proportional to $N^{1/3}$ (obtained by $N\times N^{-2/3}$, accounting for the N-dependence of the number of nanodomain facets, $\propto N$, and of their surfaces, $\propto v^{2/3}$, respectively), balancing contributions different in sign, and in functional dependence on N, may result in a T-dependent stabilization. As the boundary network creation, occurring by coherent shifts/rotations of neighboring octahedra, likely possess a negligible activation energy, its formation enthalpy must be high enough to reduce the network at low T's so as to make large enough γ domains to appear in the diffraction patterns; differently, at high(er) T's, the *negative* –TS term associated to the entropy increase more than offsets the effect of the energy needed to create many new boundaries. Summarizing, it is the different functional dependence of H and TS on N (linear and negative for –TS, and cubic root and positive for H), which can drive the formation, or fading, of this 3D moving mesh of twin boundaries.

7. Small Angle X-Ray Scattering

The SAXS data were recorded with an instrument at Aarhus University, a NanoSTAR from Bruker AXS equipped with a liquid metal jet source from Excillum AB, Sweden, and with homebuilt scatterless slits.[18,19] A homebuilt flow-through quartz capillary sample cell was used for the measurements. The data are displayed as a function of the modulus of the scattering vector $q = 4\pi \sin(\theta)/\lambda$, where 2θ is the scattering angle and λ is the x-ray wavelength.

The scattering from the samples resembles the scattering from polydisperse spheres, however, the behavior of the data for $q \rightarrow 0$ follows approximately $1/q$ suggesting that there are linear objects (strings) in the samples.

The scattering from polydisperse solid spheres is described by:[20]

$$I(q) = \Delta\rho^2 \int_0^\infty n(R)V(R)^2\, P(qR)dR$$

where $\Delta\rho$ is the excess scattering length density of the spheres,

$$n(R) = \frac{1}{R\sqrt{2\pi\sigma^2}} \exp\left(-\frac{(\ln(R) - \ln(R_a))^2}{2\sigma^2}\right)$$

is a lognormal number size distribution with the width σ and the center R_a, $V(R) = \frac{4\pi}{3}R^3$ is the volume of a sphere with radius R, and $P(qR)$ is the form factor of this sphere:

$$P(qR) = \left(\frac{3(\sin(qR) - qR\cos(qR))}{(qR)^3}\right)^2$$

The string-like organization of the particles also has to be taken into account. For monodisperse spheres a string with N spheres with separation d has the scattering:

$$I(q) = P(qR)S(q,N,d)$$

where

$$S(q,N,d) = 1 + \frac{2}{N}\sum_{j=1}^{N-1}(N-j)\frac{\sin(qjd)}{qjd}$$

is the structure factor of the string. In order to be able to fit the number of spheres in the string, the effective structure factor is introduced:

$$S_{eff}(q,a,d) = (1-w)S(q,N,d) + wS(q,N+1,d)$$

where N is the larger integer smaller than a and $w = a - N$.

To include polydispersity of the spheres in the string-like structure an approximate approach based on the local-monodisperse approximation was used:[21]

$$I(q) = \Delta\rho^2 \int_0^\infty n(R)V(R)^2\, P(qR)S_{eff}(q,a,k2R)dR$$

where k is also a fit parameter that allows for compensation of the correlation peak that the approximation might introduce.

Full outcome of the SAXS data analysis on $CsPbCl_3$ e $CsPbBr_3$ colloidal NCs follows:

	$CsPbCl_3$	$CsPbBr_3$
<*D*> (nm)	5.62(7)	7.65(4)
σ/<*D*>	0.20(1)	0.16(2)
Δ	1.055(9)	0.84(4)
n-SPH	50*	6.0(8)

*fixed (no sensitivity of the fit beyond this value)

where <*D*> and σ/<*D*> are the average NCs diameter and size dispersion, respectively, *Δ* is the refined separation between the centre of the spheres in the strings (normalized to <*D*>) and *n*-SPH is the number of spheres per string, used in the model.

The SAXS fits of the experimental data (shown in the main text, Figure 5c for $CsPbCl_3$ and 5d for $CsPbBr_3$) were performed using 100 equidistant points on the R scale between $\log(R_a)-3\sigma$ and $\log(R_a)+3\sigma$.

$CsPbCl_3$ experimental data were fitted only in the q range from 0.02 $Å^{-1}$ and upwards due to the upturn at low q (Figure 5c), which probably originates from clustering of the strings.

The separation between the spheres (*Δ*, in the Table above) for $CsPbBr_3$ is less than two times the NCs radius, which may be a consequence of the stacking of oblate structures (shorter along the string axis than perpendicular to it). Another explanation (in agreement with the DSE results, shown in the main text) can be that the particles have a cubic shape: in this case the distribution of scattering mass is further away from the centre so that two times the effective radius is larger than the cube centre-to-centre distance.

For $CsPbCl_3$ the intra-sphere distance is a bit larger than two times the sphere radius: this may indicate that these particles are more elongated along the string axis than perpendicular to it.

Supplementary Figures

Figure S1. Rietveld best fits of synchrotron data collected at the X04SA-MS4 at SLS ((λ =0.565468Å) on $CsPbCl_3$, $CsPbBr_3$ and $CsPbI_3$ samples. $CsPbCl_3$ data at 133K (a) were modelled using the *Pbnm* orthorhombic structure, data at 223 K (b) and RT (c) using the *Pm-3m* cubic structure. $CsPbBr_3$ colloidal (d) and powder (e) data, and $CsPbI_3$ colloidal data (g) at RT were modelled using the *Pbnm* orthorhombic structure; $CsPbBr_3$ data at 410K using the *Pm-3m* cubic structure (f). Experimental data: black dots, calculated patterns: green traces, difference plots: red lines.

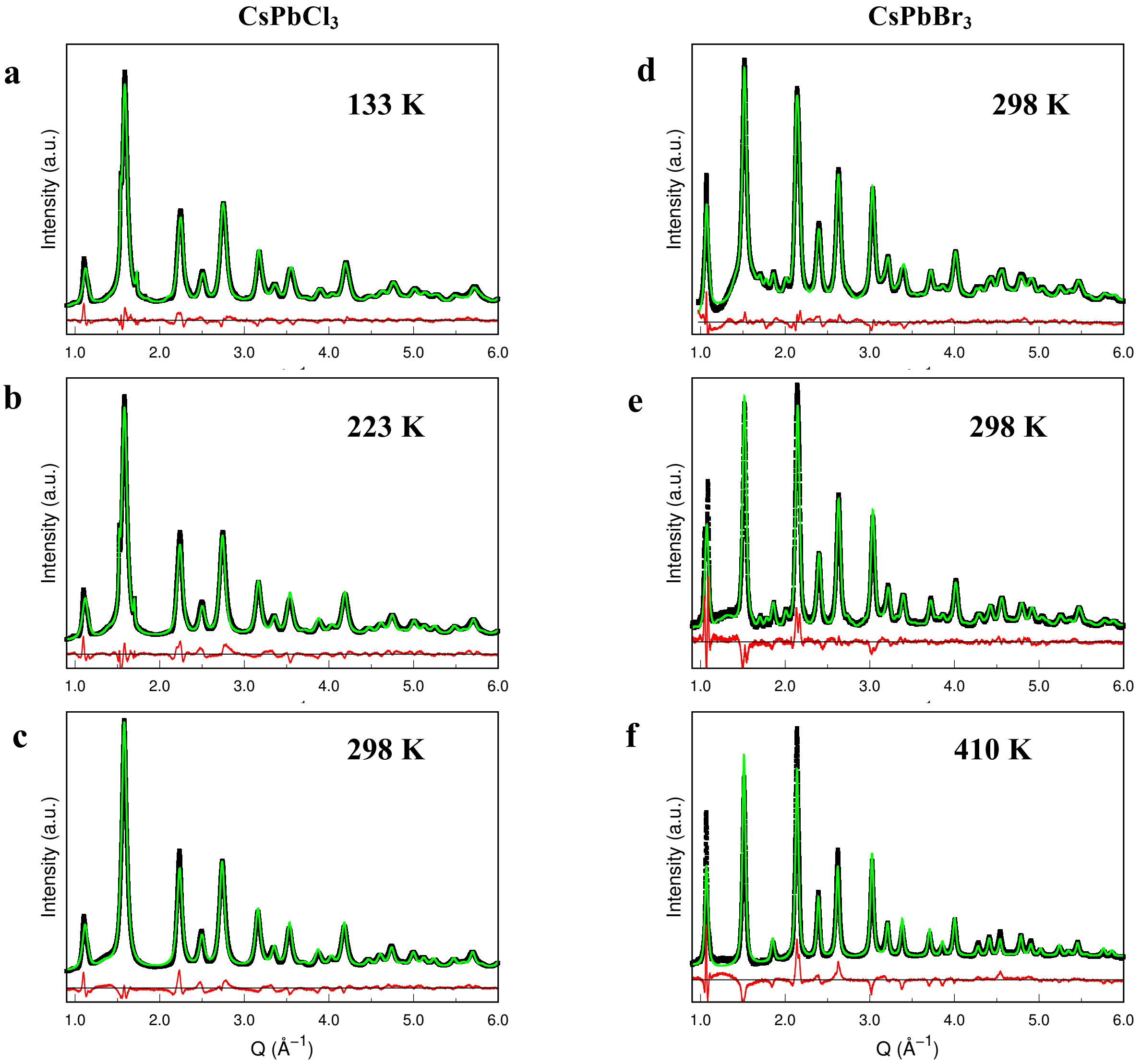

$CsPbI_3$

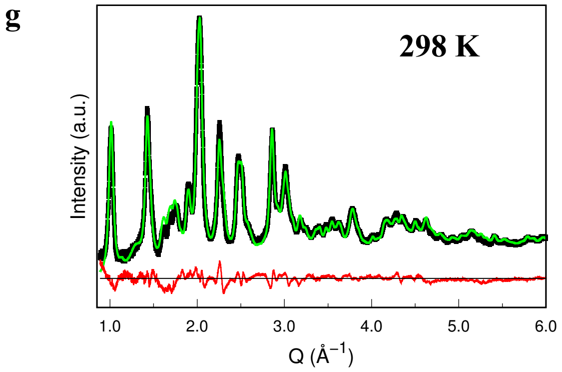

Figure S2. Analysis of the peak positions, obtained by profile fitting, of $CsPbCl_3$ RT (top) and $CsPbBr_3$ HT (bottom) data. The reflections with even $h^2+k^2+l^2$ values are distributed around a well-defined cell parameter (5.618 Å and 5.866 Å, respectively, red dashed lines), while the odd ones are significantly shifted away from the red dashed lines, suggesting a *non-cubic* metric of the lattice for both perovskites.

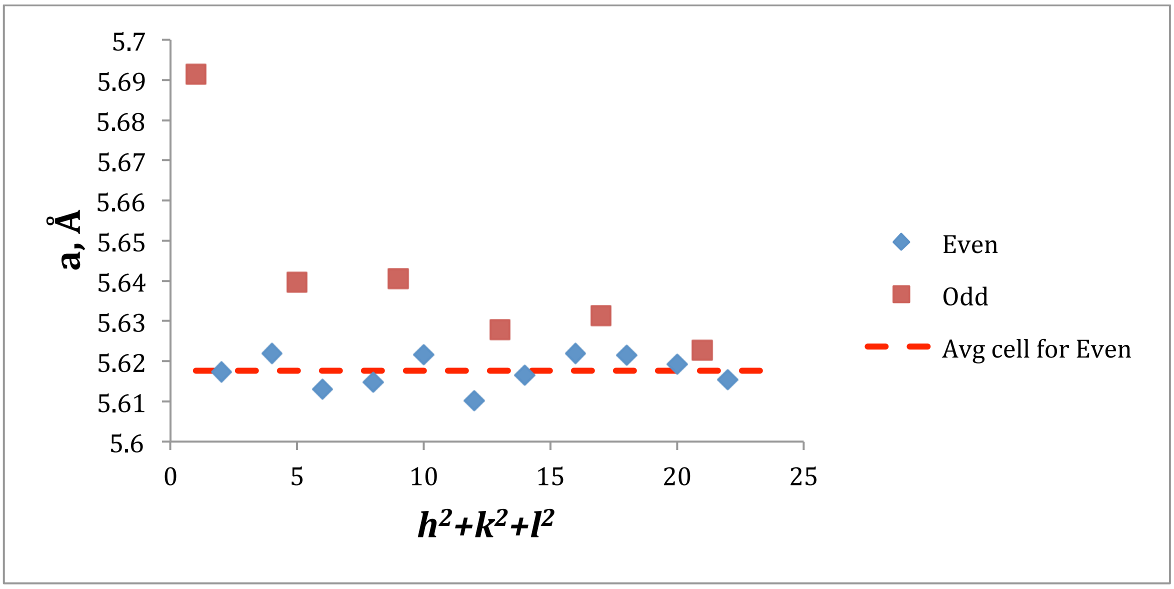

$CsPbCl_3$

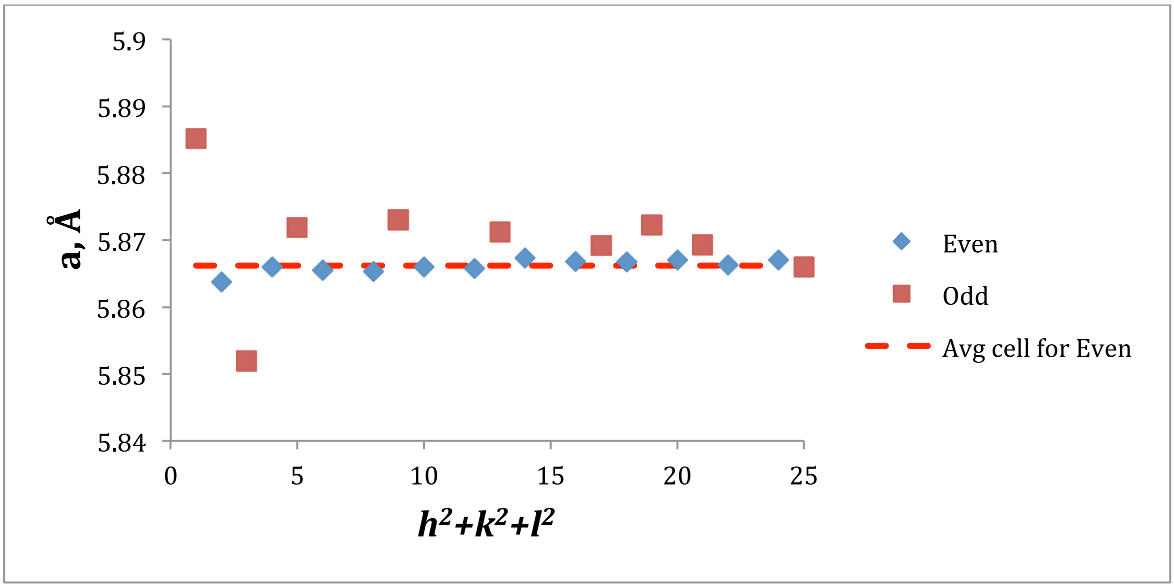

$CsPbBr_3$

Figure S3. DSE best fits (green traces) of synchrotron data (λ =0.565468Å, black dots) collected on $CsPbCl_3$ (a-c) and $CsPbBr_3$ (d-f) NCs. Data of $CsPbCl_3$ at RT, apparently cubic, were modelled using lower symmetry structures: (a) the tetragonal *P4/mbm,* (b) the *Pbnm* orthorhombic and (c) the *P2₁/m* monoclinic structures. Data of $CsPbBr_3$ at RT were modelled using the (d) *Pbnm* orthorhombic structure; data of $CsPbBr_3$ at HT were modelled using the (e) *Pm-3m* cubic and the (f) *Pbnm* orthorhombic structures, respectively (all models refer to untwinned NCs). The left-side insets showing the lowest-Q peak highlight its asymmetric shape, not recovered by symmetry lowering, and suggest the occurrence of additional crystal defectiveness of second order compared to the nanotwin boundaries. The right-side insets highlight the superstructure peaks region.

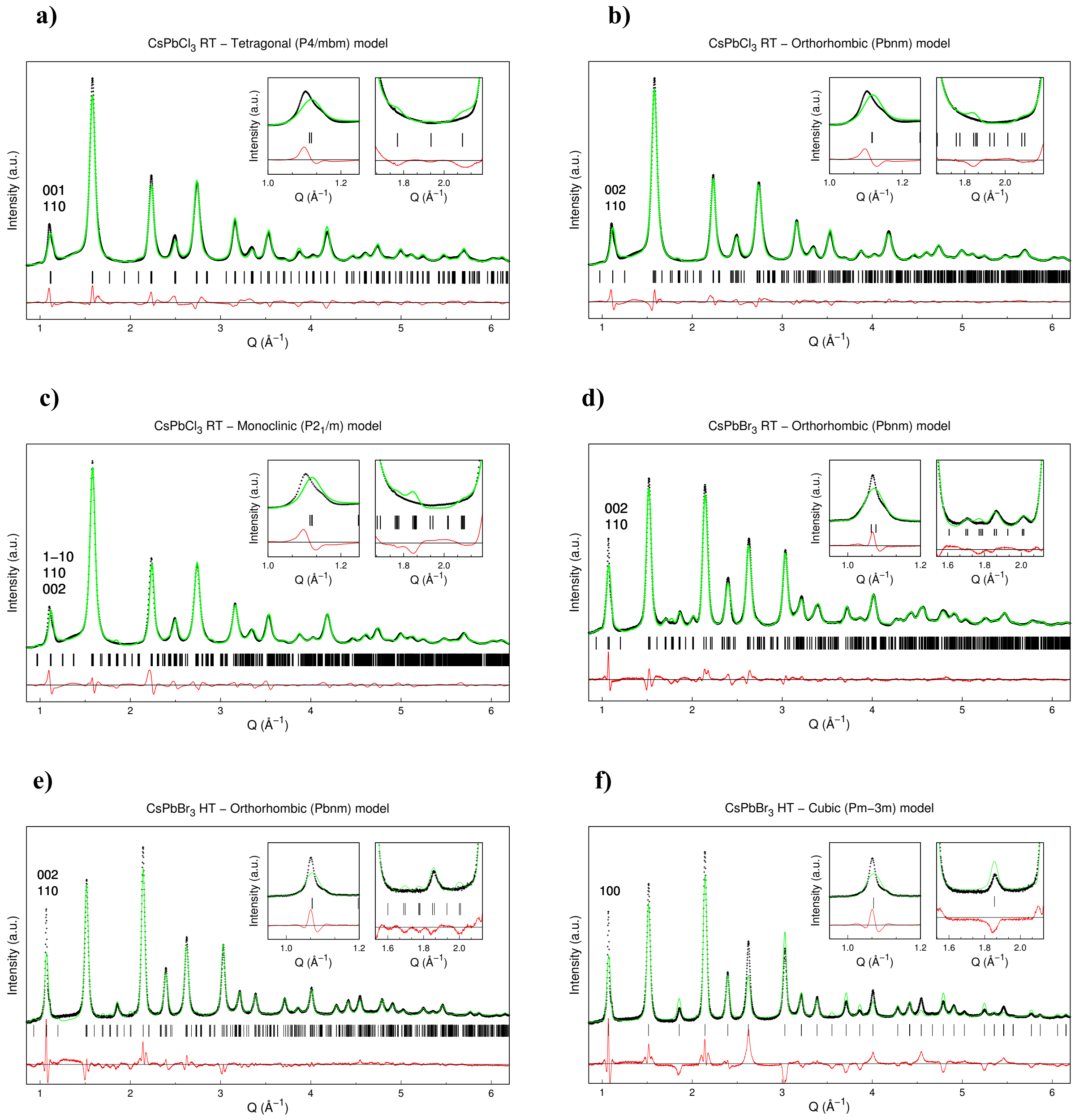

Figure S4. DSE simulations showing the selective effect of different slip geometries on the superstructure peaks of the orthorhombic *Pbnm* structure in CsPbBr3. Simulations (green traces) are compared to RT experimental data (black dots) and correspond to the untwined structure (a) and the sequence of slip geometries: $\frac{1}{2} < 110 > \{110\}$ (b), $\frac{1}{2} < 100 > \{001\}$ (c) and $\frac{1}{2} < 110 > \{001\}$ (d).

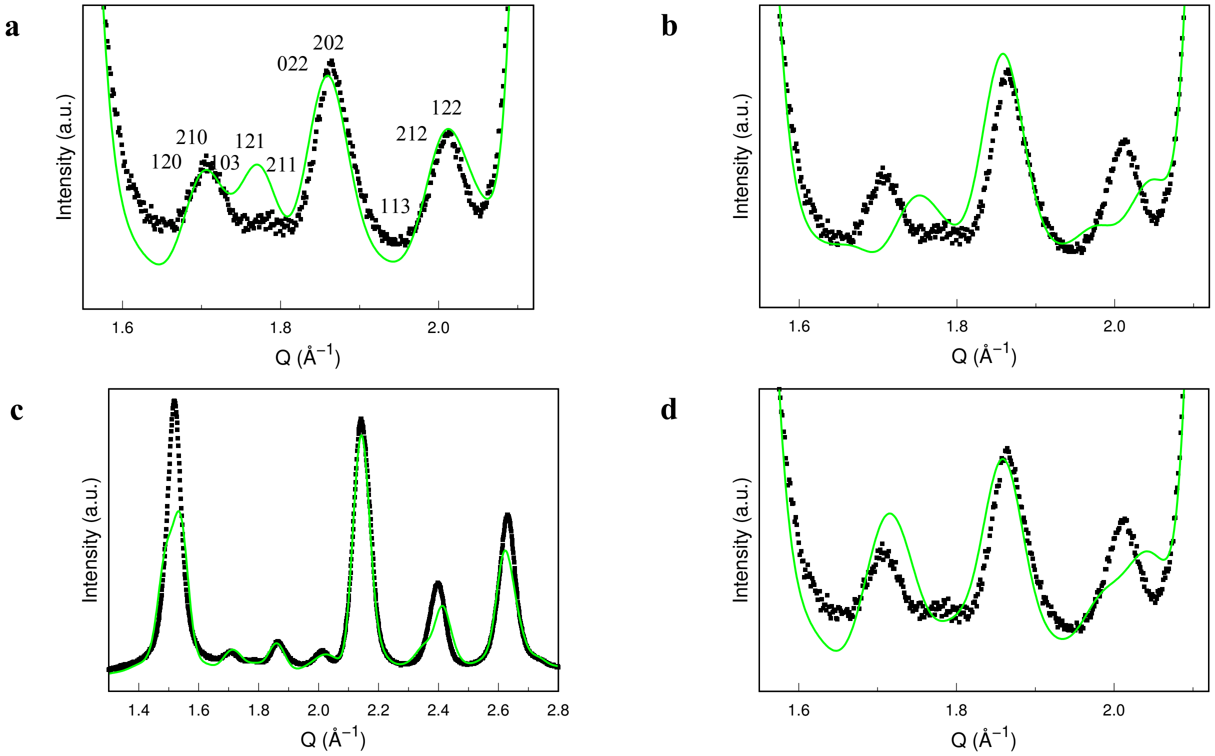

Figure S5. a) Partial PDFs of RT $CsPbBr_3$ NCs computed by PDFGui using the orthorhombic structural model, showing that the narrow peak at ~ 6 Å (close to the ideal lattice periodicity) is dominated by Pb⋯Pb contacts; b) breakdown of the Br⋯Br contributions showing the effect on partial PDFs due to the octahedral tilts. This symmetry lowering implies a marked inequivalence of the Br⋯Br pairs smearing their contribution in the 4÷7 Å range

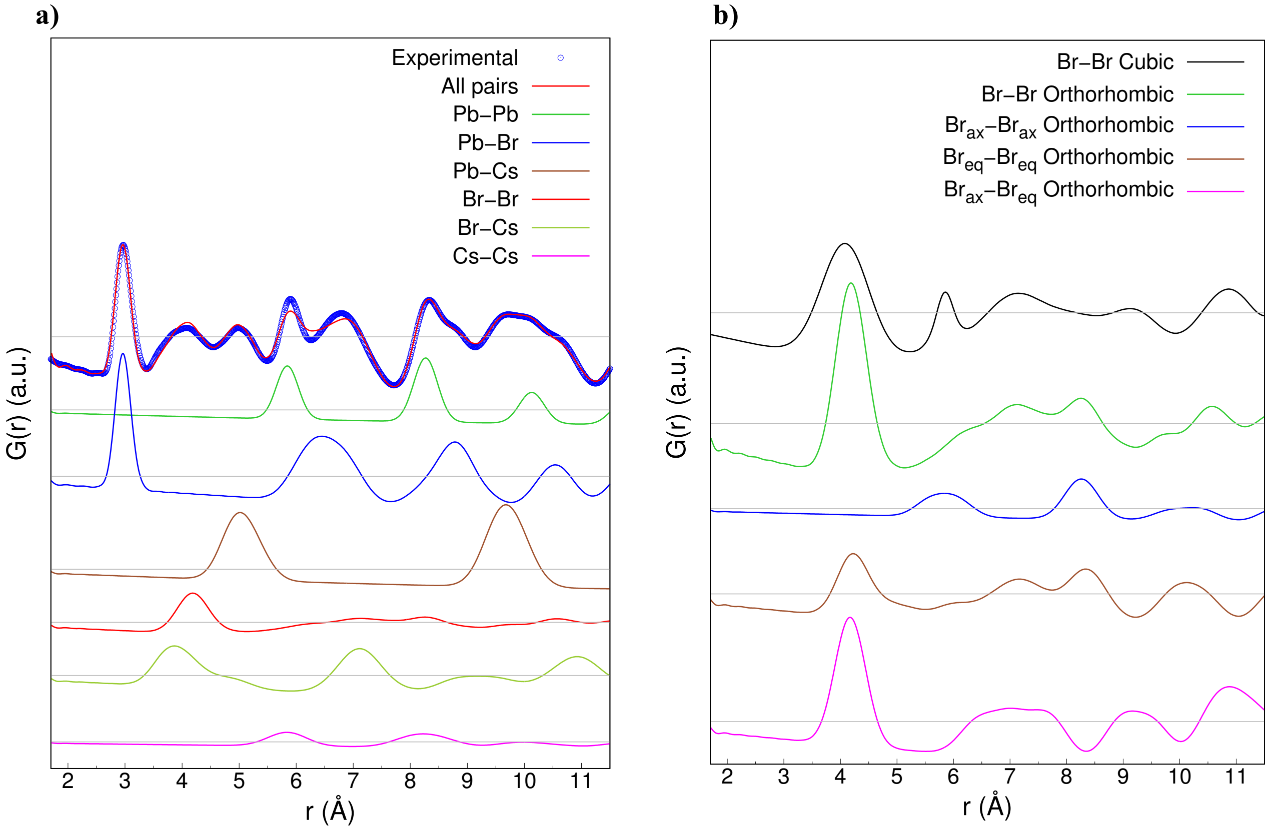

Figure S6. DSE simulation of $CsPbI_3$ NCs corresponding to the orthorhombic nanotwin model shown in the inset, resulting into a pseudo-cubic pattern. Vertical bars indicate the Bragg peaks position in the cubic α-phase.

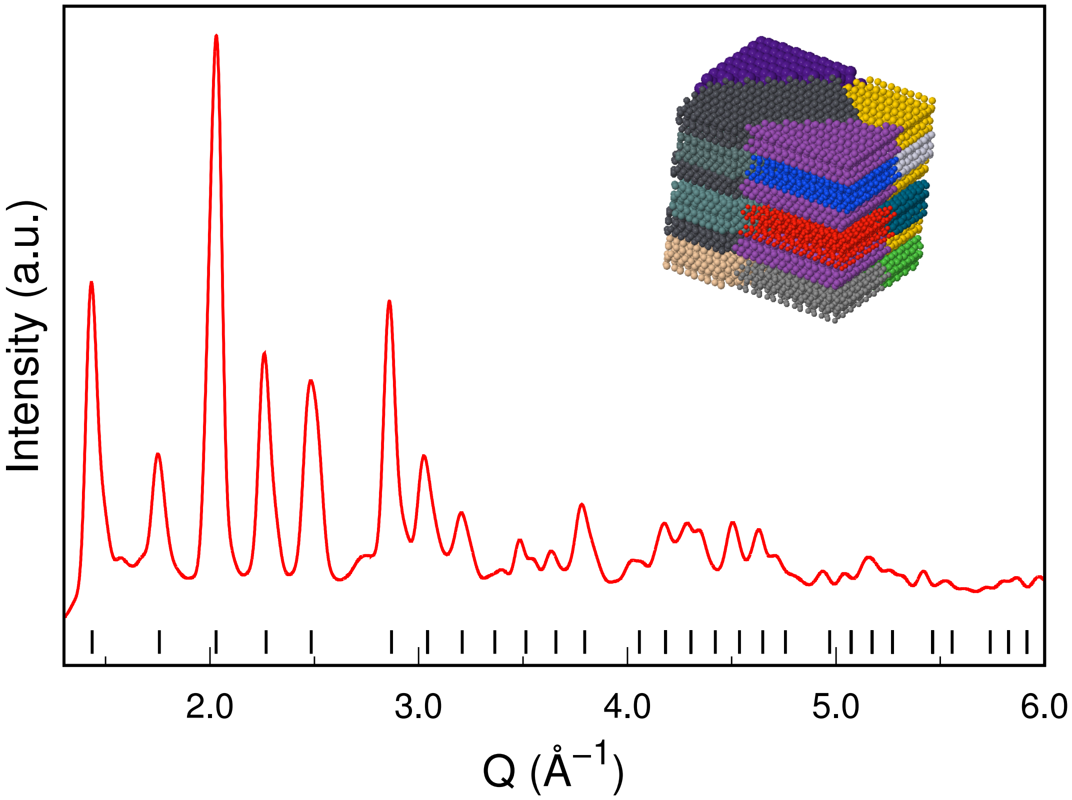

Figure S7. RT photoluminescence (PL) spectra for $CsPbCl_3$ (blue), $CsPbBr_3$ (green) and $CsPbI_3$ NCs (brown), measured in toluene solution (10mg/mL);

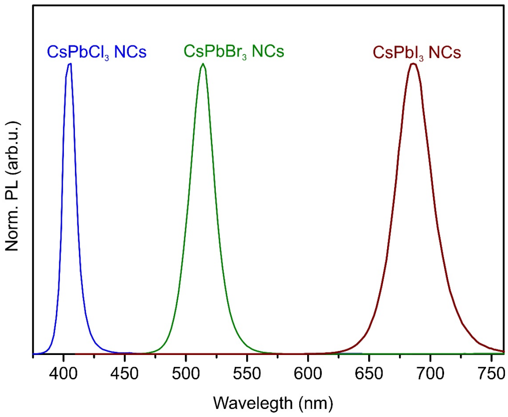

Figure S8. a) T-dependence of PL in polymer-encapsulated CsPbBr3 NCs films, monotonically decreasing from RT up to 100 °C; b) normalized PL peak intensity and (c) peak shift on heating (black) and cooling (red). The intensity and PL maximum position changes with temperature are almost reversible.

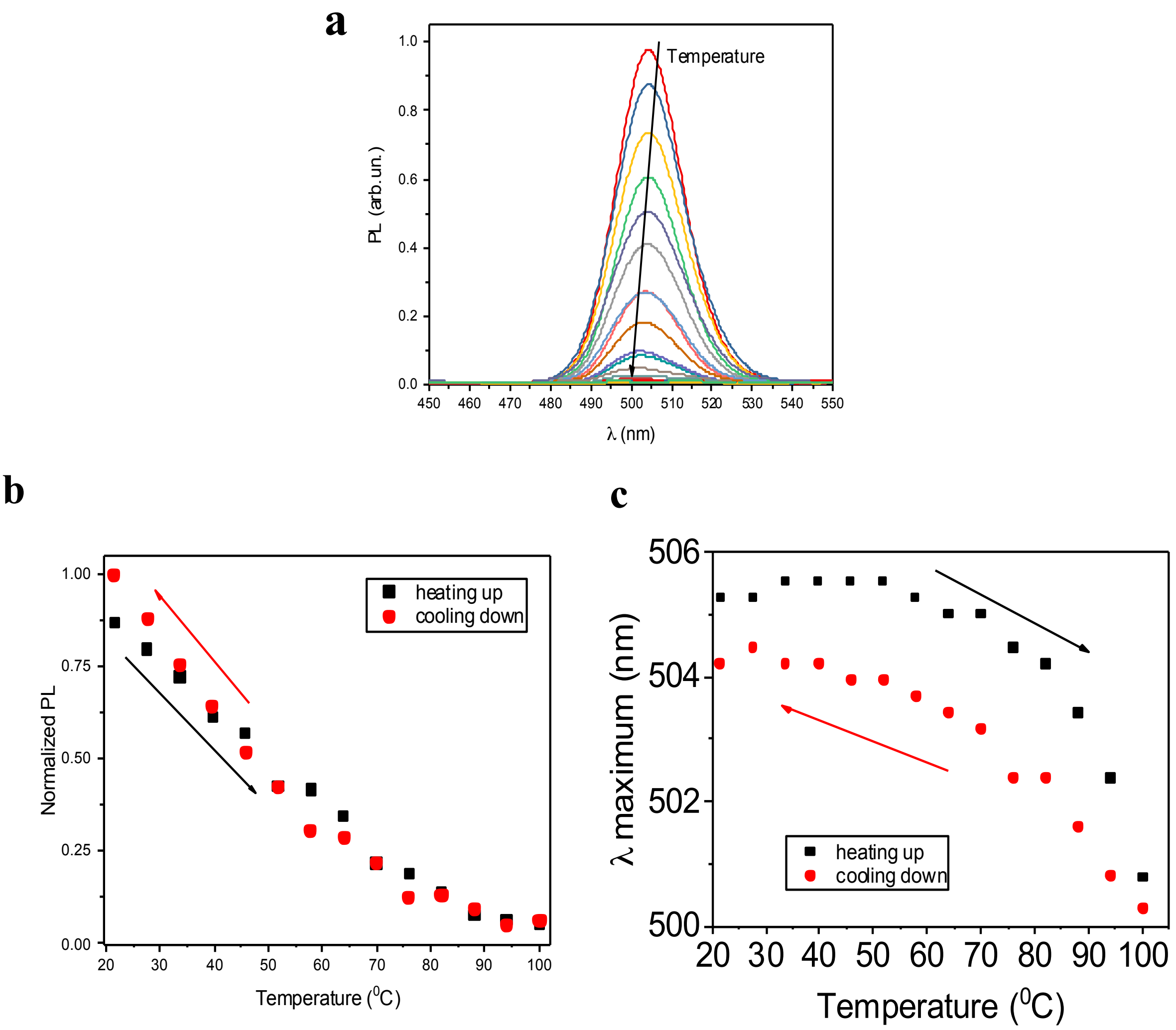

Supplementary Tables

Table S1. Rietveld refinement results using different structural models for $CsPbCl_3$ dry sample (298 K)

	Cubic (unsplit)	Cubic (split)	Tetragonal	Orthorhombic
Space Group	Pm-3m (No. 221)	Pm-3m (No. 221)	P4/mbm (No. 127)	Pbnm (No. 62)
a, Å	5.6219	5.6220	7.9334	7.8967
b, Å	= a	= a	=a	7.9834
c, Å	= a	= a	5.6260	11.2524
Z	1	1	2	4
V, Å^3	177.69	177.69	354.09	709.38
ρ_{calc}, g cm^{-3}	4.172	4.172	4.187	4.180
Pb (x,y,z)	0, 0, 0	0, 0, 0	0, 0, 0	½, 0, 0
Cs (x,y,z)	½,½,½	½,½,½	0,½,½	0.0234(3), 0.0313(6), 0.25
Cl_1 (x,y,z)	½, 0, 0	½, 0.0903(4), 0	0,0,½	0.0589(3), 0.5225(4), 0.25
Cl_2 (x,y,z)	-	-	0.1959(3), 0.6959(3), 0	0.7902(2), 0.2040(2), 0.0178(2)
B(Pb), Å^2	2.20(1)	2.32(1)	2.14(2)	2.37(1)
B(Cs), Å^2	7.84(3)	7.90(3)	6.95(3)	4.98(9)
B(Cl_1), Å^2	9.19(7)	1.85(7)	2.49(13)	1.83(5)**
B(Cl_2), Å^2	-	-	1.48(8)	1.83(5)**
R_{wp}, %	5.18*	4.25*	4.84	4.57
2θ-range, °	4-60	4-60	4-60	4-60

* A phenomenological peak shift correction was introduced for even-even-odd *hkl*'s in the form of $\Delta 2\theta = p/\cos\theta$, with $p = -0.0466(5)$; ** Constrained values. Unconstrained values are: Cl_1= 1.02(16), Cl_2 = 2.71(11)

Table S2. Rietveld refinement results for $CsPbCl_3$ dry sample at low temperatures ($\leq$ 298 K)

T, K	298	223	183	133	133
Crystal system	Cubic	Cubic	Cubic	Cubic	Orthorhombic
Space group	*Pm-3m*	*Pm-3m*	*Pm-3m*	*Pm-3m*	*Pbnm*
a, Å	5.6228(1)	5.6132(1)	5.6046(1)	5.5949(1)	7.8192(1)
b, Å					7.9203(1)
c, Å					11.2863(1)
V, Å^3	177.77(1)	176.86(1)	176.05(1)	175.14(1)	698.97(8)
Z	1	1	1	1	4
ρ_{calc}, g cm^{-3}	4.170	4.192	4.211	4.233	4.243
B(Pb), Å^2	2.56(2)	2.45(2)	2.40(2)	2.27(2)	1.84(1)
B(Cs), Å^2	8.23(3)	7.84(4)	7.68(4)	7.57(4)	6.00(6)
B(Cl), Å^2	9.61(7)	10.64(10)	11.15(10)	11.711(11)	1.28(5)*
p, °	−0.046(1)	−0.047(1)	−0.045(1)	−0.045(1)	–
R_p	0.041	0.049	0.051	0.053	0.033
R_{wp}	0.051	0.062	0.064	0.066	0.043
R_{Bragg}	0.024	0.023	0.023	0.025	0.015

* Constrained for the two crystallographically independent Cl atoms

Table S3. Rietveld refinement results for colloidal $CsPbBr_3$ and $CsPbI_3$ (298 K), $X_1 = X_{ax}$, $X_2 = X_{eq}$.

	$CsPbBr_3$	$CsPbI_3$
Space Group	Pbnm (No. 67)	Pbnm (No. 67)
a, Å	8.2105(7)	8.6124(6)
b, Å	8.2829(7)	8.8454(6)
c, Å	11.8039(6)	12.5243(7)
Z	4	4
V, $Å^3$	802.74	954.10
ρ_{calc}, g cm^{-3}	4.798	5.018
Pb (x,y,z)	½, 0, 0	½, 0, 0
Cs (x,y,z)	0.0040(11), 0.0061(7), 0.25	0.9801(6), 0.9473(4), 0.25
X_1 (x,y,z)	−0.0386(3), 0.4732(5), 0.25	0.0566(4), 0.5084(6), 0.25
X_2 (x,y,z)	0.7951(2), 0.2061(3), 0.0236(1)	0.8070(3), 0.1968(3), 0.0236(2)
B(Pb), $Å^2$	2.03(2)	3.12(4)
B(Cs), $Å^2$	8.11(5)	8.54(13)
$B(X_1)$, $Å^2$	1.21(7)	5.21(13)
$B(X_2)$, $Å^2$	3.65(5)	3.75(6)
R_{wp}, %	4.43	6.29
2θ-range, °	5-60	4-50
$a_{eq} = (V/Z)^{1/3}{}_{,}$ Å	5.8569	6.2017
Δ, % (∗)	1.2	2.2
Pb-$X_{1, ,}$Å	2.976	3.170
Pb-$X_{2, ,}$Å	2.972, 2.977	3.169. 3.180
Pb-X_1-Pb, °	165.0(1)	162.1(1)
Pb-X_2-Pb, °	157.2(1)	153.0(1)
cis-X_2-Pb-X_2, °	88.4(1), 91.6(1)	88.7(1), 91.3(1)
min. Cs$\cdots$X distance, Å	3.60	3.89

(∗) Δ, % = 100 × $[(a-a_{eq})^2 +(b-a_{eq})^2 + (c-a_{eq})^2]^{1/2}$ is an estimate of the distortion from the cubic perovskitic cell, with edges taken as a_{eq}., manifestly larger in $CsPbI_3$ than in $CsPbBr_3$

Table S4. Statistical indicators, in the form of Goodness of Fit (GoF) and weighted profile agreement factor (R_{wp}, values x 100) obtained by refining, on synchrotron X-ray diffraction data, different structural models (periodic and twinned) using different methods (DSE-based, Rietveld). The indicators refer to some of the $CsPbX_3$ samples described in the main text: $CsPbCl_3$ at RT in gel (G), $CsPbBr_3$ at RT and HT, in colloidal (C) and powder (P) forms, and colloidal $CsPbI_3$ at RT). The absolute values of GoF systematically depend on the counting rates, which are order of magnitudes different due to the distinct data collection in separate sessions.

SG = Space Group; N_{par} = number of free metric, structural and microstructural variables. Direct comparison of these indicators is not straightforward due to the different modelling conditions. Rietveld fits were performed neglecting data above 11 Å^{-1} in Q, owing to the absence of Bragg peaks. In DSE modelling, using full data is highly recommended in order to stabilize the rescaling of the solvent signal (in the case of colloidal samples) and to separate the Compton (inelastic scattering) in a more accurate manner; therefore refinement was performed over the 0.3-11 Å^{-1} Q range.

	Ordered Model							Twinned Model		
	Rietveld				**DSE**			**DSE**		
	Q-range = 0.3–11 Å^{-1}				Q-range = 0.3- 19 Å^{-1}			Q-range = 0.3- 19 Å^{-1}		
	SG	**GoF**	**R_{wp}**	**N_{par}**	**GoF**	**R_{wp}**	**N_{par}**	**GoF**	**R_{wp}**	**N_{par}**
RT $CsPbCl_3$ (G)$^{\#}$	*Pm-3m*	15.57	6.23	7	12.14	5.76	7	10.10	4.79	7
RT $CsPbBr_3$ (C)	*Pbnm*	3.22	5.43	17	2.08	0.89	7	1.99	0.86	7
HT $CsPbBr_3$ (P)	*Pm-3m*	3.83	11.47	7	3.07	10.28	7	2.26	7.58	7
RT $CsPbI_3$ (C)$^{\#\#}$	*Pbnm*	2.12	6.44	17	3.08	0.82	7	-	-	-

$^{\#}$ DSE modelling performed in the 0.3-17 Å^{-1} Q-range; $^{\#\#}$ DSE modelling performed in the 0.3-13 Å^{-1} Q-range.

Table S5. The most relevant structural parameters provided by PDF and DSE analyses for the $CsPbBr_3$ dry powder.

	PDF		**DSE**	
	Tetragonal	Orthorhombic	Tetragonal	Orthorhombic
Space Group	P4/mbm (No. 127)	Pbnm (No. 62)	P4/mbm (No. 127)	Pbnm (No. 62)
a, Å	8.2509	8.1998	8.2458	8.1980
b, Å	= a	8.3381	= a	8.3108
c, Å	5.8887	11.7258	5.9002	11.8073
B(Pb), Å^2	2.03	1.80	2.24	1.88
B(Cs), Å^2	8.23	5.12	9.18	8.04
B(Br_1), Å^2	6.82	3.14	7.24	1.35
B(Br_2), Å^2	4.85	4.69	3.23	2.76

References

(1) Protesescu, L.; Yakunin, S.; Bodnarchuk, M.I.; Krieg, F.; Caputo, R.; Hendon, C.H.; Yang, R.X.; Walsh, A.; Kovalenko, M.V. Nanocrystals of Cesium Lead Halide Perovskites ($CsPbX_3$, X = Cl, Br, and I): Novel Optoelectronic Materials Showing Bright Emission with Wide Color Gamut. *Nano Lett.* **2015**, *15*, 3692-3696.

(2) Willmott, P. R.; Meister, D.; Leake, S. J.; Lange, M.; Bergamaschi, A.; Böge, M.; Calvi, M.; Cancellieri, C.; Casati, N.; Cervellino, A.; Chen, Q.; David, C.; Flechsig, U.; Gozzo, F.; Henrich, B.; Jäggi Spielmann, S.; Jakob, B.; Kalichava, I.; Karvinen, P. *et al. J.* The Materials Science Beamline Upgrade at the Swiss Light Source. *Synchrotron Rad.* **2013**, *20*, 667-682.

(3) Bergamaschi, A.; Cervellino, A.; Dinapoli, R.; Gozzo, F.; Henrich, B.; Johnson, I.; Kraft, P.; Mozzanica, A.; Schmitt, B.; Shi, X. The MYTHEN Detector for X-ray Powder Diffraction Experiments at the Swiss Light Source. *J. Synchrotron Rad.* **2010**, *17*, 653-668.

(4) Paalman, H. H.; Pings, C. J. Numerical Evaluation of X-Ray Absorption Factors for Cylindrical Samples and Annular Sample Cells. *J. Appl. Phys.* **1962**, *33*, 2635-2639.

(5) Hutton, J.; Nelmes, R. J.; Meyer, G. M.; Eiriksson, B. R. High-Resolution Studies of Cubic Perovskites by Elastic Neutron Diffraction: $CsPbCl_3$. *J. Phys. C* **1979**, *12*, 5393-5410.

(6) Rodova, M.; Brozek, J.; Knizek, K.; Nitsch, K. Phase Transitions in Ternary Caesium Lead Bromide. *J. Therm. Anal. Calorim.* **2003**, *71*, 667-673

(7) Diehm, P.M.; Agoston, P.; Albe, K. Size-Dependent Lattice Expansion in Nanoparticles: Reality or Anomaly? *ChemPhysChem* **2012**, *13*, 2443-2454

(8) Cervellino, A; Frison, R.; Bertolotti, F.; Guagliardi A. DEBUSSY 2.0: the New Release of a Debye User System for Nanocrystalline and/or Disordered Materials. *J. Appl. Cryst.* **2015**. *48*, 2026-2032.

(9) Cervellino, A.; Giannini, C.; Guagliardi, A. On the Efficient Evaluation of Fourier Patterns for Nanoparticles and Clusters. *J. Comput, Chem.* **2006**, *27*, 995-1008.

(10) Sampson, P. D.; Siegel, A. F. The Measure of "Size" Independent of "Shape" For Multivariate Lognormal Populations. *J. Am. Stat. Assoc.* **1895**, *80*, 910-914.

(11) Nelder, J. A.; Mead, R. A Simplex Method for Function Minimization. *Comput. J.* **1965**, *27*, 308–313.

(12) Bertolotti, F; Moscheni, D.; Migliori, A.; Zacchini, S.; Cervellino, A.; Guagliardi A.; Masciocchi, N. A Total Scattering Debye Function Analysis Study of Faulted Pt Nanocrystals Embedded in a Porous Matrix. *Acta Cryst.* **2016**, *A72*, 632-644.

(13) Wang, Y.; Guyot, F.; Yeganeh-Haeri, A.; Liebermann, R. C. Twinning in $MgSiO_3$ Perovskite. *Science*, **1990**, *248*, 468–471.

(14) Chupas, P. J.; Qiu, X.; Hanson, J. C.; Lee, P. L.; Grey, C. P.; Billinge, S. J. L. *J.* Rapid-Acquisition Pair Distribution Function (RA-PDF) Analysis. *Appl. Cryst.* **2003**, *36*, 1342-1347.

(15) Juhas, P.; Davis, T.; Farrow, C. L.; Billinge, S. J. L. PDFgetX3 : a Rapid and Highly Automatable Program for Processing Powder Diffraction Data into Total Scattering Pair Distribution Functions. *J. Appl. Cryst.* **2013**, *46*, 560-566.

(16) Farrow, C. L.; Juhas, P.; Liu, J. W.; Bryndin, D.; Božin, E. S.; Bloch, J.; Proffen, T.; Billinge, S. J. L. PDFfit2 and PDFgui: Computer Programs for Studying Nanostructure in Crystals. *J. Phys. Condens. Matter* **2007**, *19*, 335219.

(17) Gilbert, B. Finite Size Effects on The Real-Space Pair Distribution Function of Nanoparticles. *J. Appl.*

Cryst. **2008**, *41*, 554-562.

(18) Li, Y.; Beck, R.; Huang, T.; Choi, M. C.; Divinagracia, M. Scatterless Hybrid Metal–Single-Crystal Slit for Small Angle X-Ray Scattering and High-Resolution X-Ray Diffraction. *J. Appl. Cryst*. **2008**, *41*, 1134-1139.

(19) Schwamberger, A.; De Roo, B.; Jacob, D.; Dillemans, L.; Bruegemann, L.; Seo, J. W.; Locquet. J. P. Combining SAXS and DLS for Simultaneous Measurements and Time-Resolved Monitoring of Nanoparticle Synthesis. *Nucl. Instrum. Methods Phys. Res., Sect.* B **2015**, *343*, 116-122.

(20) Pedersen, J. S. Analysis of Small-Angle Scattering Data From Colloids and Polymer Solutions: Modeling and Least-Squares Fitting. *Adv. Colloid Interface Sci.* **1997**, *70*, 171-210.

(21) Pedersen, J. S. Determination of Size Distributions from Small-Angle Scattering Data for Systems with Effective Hard-Sphere Interactions. *J. Appl. Cryst.* **1994**, *27*, 595-608.